energies

MDPI

*Article*

# Proppant Transportation in Cross Fractures: Some Findings and Suggestions for Field Engineering

**Yan Zhang [1,2], Xiaobing Lu [1,2], Xuhui Zhang [1,2,*] and Peng Li [1,2]**

[1] Institute of Mechanics, Chinese Academy of Sciences, Beijing 100190, China; zhangyan162@imech.ac.cn (Y.Z.); xblu@imech.ac.cn (X.L.); lipeng@imech.ac.cn (P.L.)
[2] School of Engineering Science, University of Chinese Academy of Sciences, Beijing 100049, China
* Correspondence: zhangxuhui@imech.ac.cn; Tel.: +86-10-82544192

Received: 10 August 2020; Accepted: 18 September 2020; Published: 19 September 2020


**Abstract:** The proppant transportation is a typical two-phase flow process in a complex cross fracture network during hydraulic fracturing. In this paper, the proppant transportation in cross fractures is investigated by the computational fluid dynamics (CFD) method. The Euler–Euler two-phase flow model and the kinetic theory of granular flow (KTGF) are adopted. The dimensionless controlling parameters are derived by dimensional analysis. The equilibrium proppant height (EPH) and the ratio of the proppant mass (RPM) in the secondary fracture to that in the whole cross fracture network are used to describe the movement and settlement of proppants in the cross fractures. The main features of the proppant transportation in the cross fractures are given, and several relative suggestions are presented for engineering application in the field. The main controlling dimensionless parameters for relative EPH are the proppant Reynolds number and the inlet proppant volume fraction. The dominating dimensionless parameters for RPM are the relative width of the primary and the secondary fracture. Transportation of the proppants with a certain particle size grading into the cross fractures may be a good way for supporting the hydraulic fractures.

**Keywords:** proppant transportation; cross fractures; CFD simulation; dimensional analysis; equilibrium proppant height

## 1. Introduction

Unconventional energy resources such as low permeability, shale, and tight oil and gas reservoirs account for a larger and larger proportion in the present oil and gas exploration [1–4]. The hydraulic fractures are the main flow channel for these fluid resources due to the natural poor flow capability of the porous media, and it is of great importance to know the effective support range and the distribution of proppants in cross fractures.

Many researchers have studied the proppant transportation in the cross fractures by experiments and numerical simulations. Alotaibi and Miskimins [5] designed a cross fracture system with one primary fracture, three secondary fractures, and two tertiary fractures. They found that the proppants were able to flow into the subsidiary fractures and form a proppant bed. However, they did not realize that the proppants moved not so far in the subsidiary fractures. The transportation distance of the proppant in the subsidiary fractures is important for the production. Sahai et al. [6] investigated the effects of the fracture geometrical complexity, the pumping rates, the proppant concentration, and the proppant size on the proppant transportation. The mechanism of the proppant from the primary fracture into the secondary fracture was also analyzed. McClure [7] analyzed in detail the formation process of the equilibrium proppant height (EPH). As the proppants settle at the bottom of the fractures,

the height of the proppant bed gradually grows to EPH during transportation [7]. The velocity of the mixture of water and proppants above the proppant bed in the fractures is called the equilibrium mixture velocity (EMV) when the EPH is reached. It is worth noting that the proppant bed will be eroded if the proppant bed height is greater than the EPH. The proppant bed height decreases over time during erosion until the EPH is reached. The Euler–Lagrange method was used by Hu et al. [8] to study the proppant transportation in a single vertical fracture. They suggested that the coarse proppants may be transported first, followed by the fine proppants. The coarse proppants will form a proppant bed quickly and then the fine proppants are transported far in the fractures. Roostaei et al. [9] combined a proppant transport model with the numerical hydraulic fracture model to study the fracturing response and the effect of proppant injection on the fracture propagation and dimensions. They found that the fluid viscosity is the most important parameter on the proppant transportation.

Little attention is paid to the amount of proppants entering the secondary fracture, which is a very important quantity for the field engineering. In addition, the mechanism of the proppant moving from the primary fracture into the secondary fracture is also not well understood.

In this paper, the proppant transportation behaviors in the cross fractures are investigated in detail based on the previous work [10] of our group. The Euler–Euler two-phase flow model combined with the kinetic theory of granular flow (KTGF) approach is used. Two dimensionless parameters to describe the proppant distribution in the cross fractures are presented. The first one is the relative EPH, representing the ratio of the EPH to the height of the cross fractures. The other one is the ratio of the proppant mass (RPM) in the secondary fracture to that in the whole cross fracture network. In Section 2, the numerical model and the dimensionless parameters relative to the proppant transportation in the cross fractures are introduced. Compared to the previous work [10], the boundary conditions and the fracture width in the numerical model have been changed to capture more information of the flow behaviors and to be practical for the field engineering. In Section 3, the effects of the dimensionless parameters are analyzed. Some suggestions are given for the field engineering application based on the simulated results.

## 2. Methods

### 2.1. CFD Simulation

#### 2.1.1. Model Descriptions

The Euler–Euler two-phase flow model is used to simulate the proppant transportation in the cross fractures. This model takes the multitude of particles as an artificial solid phase that can interpenetrate the continuous water phase [11,12]. The KTGF approach is used to simulate the particle collisions. Based on the KTGF approach, an additional equation, i.e., the particle temperature equation, is solved to represent the fluctuations of the particles. This equation leads to additional terms as the particle pressure force and so on. More details about this model were detailed in the previous paper [10,13].

#### 2.1.2. Geometry and Mesh

The geometry of the cross fractures in the numerical simulation is shown in Figure 1. The cross fractures contain one primary fracture and one secondary fracture. The secondary fracture intersects the primary fracture at a certain angle (bypass angle $\theta$). It is assumed that the height of the cross fractures remains constant along the moving direction of the mixture, and the height of the primary fracture equals that of the secondary fracture. The scales of the primary fracture and secondary fracture are length × height = 1000 mm × 150 mm and 600 mm × 150 mm, respectively. The horizontal distance between the entrance of the secondary fracture and the primary fracture is 400 mm. The width and bypass angle ($\theta$) of the primary and secondary fracture are varied in different cases. The geometry references the experiment apparatus of Alotaibi and Miskimins [5], Tong and Mohanty [11], and Patankar et al. [14]. The mixture of the proppants and water enters the primary

fracture from an inlet which is simplified as a rectangular opening. In actual hydraulic fractures, the proppants are generally blocked by an unruptured stratum. That means that the front end of the cross fractures is closed. Therefore, a wall is set at the end of the geometry in the numerical model. The mixture is only permitted to flow out of the cross fractures through the outlet on the top of the wall (Figure 1). The flow field is divided into hexahedral structured cells due to the consideration of computation accuracy and convergence. A standard case is first calculated with the proppant density $\rho_s$ = 3300 kg/m$^3$, the proppant diameter $d_s$ = 0.5 mm, the water density $\rho_l$ = 1000 kg/m$^3$, the water viscosity $\mu_l$ = 0.001 Pa·s, the secondary fracture width $w_b$ = 1.5 mm, the primary fracture width $w_a$ = 5 mm, the injection velocity ($U_0$) 0.2 m/s, and inlet proppant volume fraction ($\alpha_{s0}$) 3%. To evaluate the mesh independence, three kinds of mesh with different sizes are performed. The mesh size in the height, length, and width is 4 × 4 × 1 mm (coarse), 2 × 2 × 1 mm (medium), and 2 × 2 × 0.5 mm (fine), respectively. The EPH obtained from the medium grid is similar to that from the fine grid. So, the grid size 2 × 2 × 0.5 mm is used.

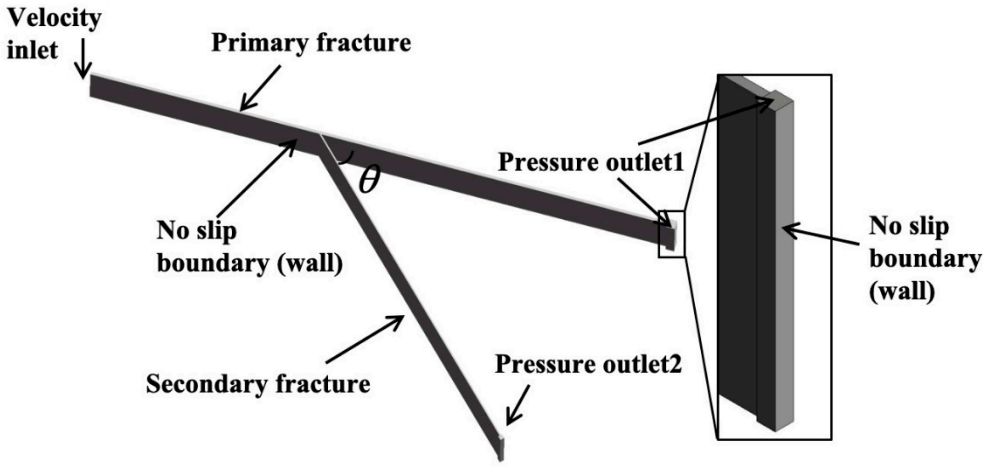


**Figure 1.** The geometry representing the cross fractures. The cross fractures consist of a primary fracture and a secondary fracture in length × height: 1000 mm × 150 mm and 600 mm × 150 mm, respectively. The width and the bypass angle will be changed in different cases.

### 2.1.3. Initial and Boundary Conditions

Initially, the cross fractures are filled with water, and then the proppants begin to enter the cross fractures. The velocity inlet is set. Different pumping flow rates and sand ratios are imposed by varying the injection rates and the inlet volume fraction of the proppants. The inner walls of the cross fractures are set as the no-slip wall boundary conditions for each phase. The pressure outlet is set to be zero gauge pressure. The values of the parameters used in the numerical simulation are listed in Table 1. The ANSYS FLUENT software is used for the numerical simulation.

**Table 1.** Parameter values in the numerical simulation.

| Parameters | Units | Value |
|---|---|---|
| Proppant diameter | mm | 0.5 |
| Water density | kg/m$^3$ | 1000 |
| Water viscosity | Pa·s | 0.001 |
| Primary fracture: length × height | mm | 1000 × 150 |
| Secondary fracture: length × height | mm | 600 × 150 |
| Size of grid: length × height × width | mm | 2 × 2 × 0.5 |

#### 2.1.4. Solution Algorithm

The phase coupled Semi-Implicit Method for Pressure Linked Equations (SIMPLE) method is used for the pressure–velocity coupling, and the Green–Gauss cell-based method is used to discretize the gradient. The equation of momentum, the particle temperature equation, the turbulent kinetic energy, and the dissipation rate equation are treated with the second-order upwind scheme. The Quadratic Upstream Interpolation for Convective Kinetics (QUICK) scheme is used to discretize the volume fraction equation.

### *2.2. Dimensional Analysis*

All the variables of the problem relating the proppant transportation in the cross fractures based on the equations and the boundary conditions are shown and explained as follows.

The variables of geometry of the cross fractures: the width of the primary fracture and the secondary fracture ($w_a$ and $w_b$), the length of the primary and the secondary fracture ($L_a$ and $L_b$), the height of the cross fractures ($H$), the distance from the secondary fracture to the primary fracture entrance ($l$), and the angle between the primary and secondary fracture (bypass angle $\theta$).

The variables of physical properties of the proppant and water: the density of the proppant and the water ($\rho_s$ and $\rho_l$), the average diameter of the proppant ($d_s$), and the viscosity of the water ($\mu_l$).

The variables relating the boundary conditions: the injection velocity of the mixture ($U_0$), the inlet volume fraction of the proppant ($\alpha_{s0}$), and the gravity acceleration $g$.

Two parameters to evaluate the quality of hydraulic fracturing are introduced. The first one is the EPH in the primary fracture, and the other one is the RPM. The EPH in the cross fractures is discussed by many researchers [5,13,15,16]. The EPH and the RPM can be written as a causal function of the above variables:

$$(h, R) = f(\alpha_{s0}, U_0, g; \theta, w_a, w_b, L_a, L_b, l, H; \rho_s, d_s, \rho_l, \mu_l) \quad (1)$$

where $h$ and $R$ are the EPH and the RPM, respectively. The dimensionless causal relationship can be written as [17]:

$$\left(\frac{h}{H}, R\right) = f\left(\alpha_{s0}, Re, Ar, \theta, \frac{w_a}{d_s}, \frac{w_b}{d_s}, \frac{L_a}{d_s}, \frac{L_b}{d_s}, \frac{l}{d_s}, \frac{H}{d_s}, \frac{\rho_s}{\rho_l}\right) \quad (2)$$

in which $h/H$ is the relative EPH, $Re = \rho_l d_s U_0/\mu_l$ is the proppant Reynolds number, $Ar = (\rho_s - \rho_l)\rho_l d_s^3 g/\mu_l^2$ is the Archimedes number, $w_a/d_s$ and $w_b/d_s$ are the relative width of the primary and secondary fracture, $L_a/d_s$ and $L_b/d_s$ are the relative length of the primary and secondary fracture, $l/d_s$ is the relative distance of the secondary fracture to the primary fracture entrance, $H/d_s$ is the relative height of the cross fractures, and $\rho_s/\rho_l$ is the ratio of the proppant density to the water density. Here, the relative length and height of the cross fractures as well as the density ratio of the proppant to water are constant. Equation (2) can be rewritten as:

$$\left(\frac{h}{H}, R\right) = f\left(\alpha_{s0}, Re, Ar, \theta, \frac{w_a}{d_s}, \frac{w_b}{d_s}, \frac{l}{d_s}\right). \quad (3)$$

The effect of the controlling dimensionless independent variables at the left side of Equation (3) on the dependent variables is investigated in this paper. Table A1 in Appendix A shows all the cases adopted in the numerical simulation. The bold part in Table A1 is the standard case. Cases 1–8 are set to study the effects of the inlet proppant volume fraction. Cases 3 and 9–13 are set to study the effects of the proppant Reynolds number. Cases 3 and 14–18 concern the effects of the Archimedes number. Cases 3 and 19–24 concern the effects of the bypass angle. Cases 3 and 25–33 are designed to study the effects of the relative width of the primary fracture and secondary fracture. Cases 3 and 34–39 are designed to study the relative distance of the secondary fracture to the primary fracture entrance.

The slick-water hydraulic fracturing is widely used in the unconventional resources [3,18]. The slick-water consists of water and chemical ingredients such as the friction reducer, the clay stabilizer, and the bactericide. These chemical additives account for no more than 1% content in slick-water. However, it plays an important role in reducing the friction of the side wall. The viscosity of the slick-water is about 0.8–1.2 mPa·s. Generally, the tap water is used instead of the slick-water in the experiment. In this paper, the tap water is also used with a constant viscosity of 0.001 Pa·s.

## 3. Results and Discussion

Figure 2 shows the deposition form of the proppant in the primary fracture at different time points (Case 3). The proppant distribution is similar to the experiment results of previous researchers [1,5,6,19,20]. The proppants first stack at a certain distance from the entrance after entering the primary fracture. The height of proppant bed increases with little change in length until the EPH is reached. Then, the transportation of proppant tends to be stable, as the height of the proppant bed remains unchanged, and the proppant bed only changes in the fracture length direction. The proppant bed at the bottom of the fracture plays an important role in supporting the fractures after the pressure is released. It resembles a stationary porous medium through which the gas and oil will be extracted.

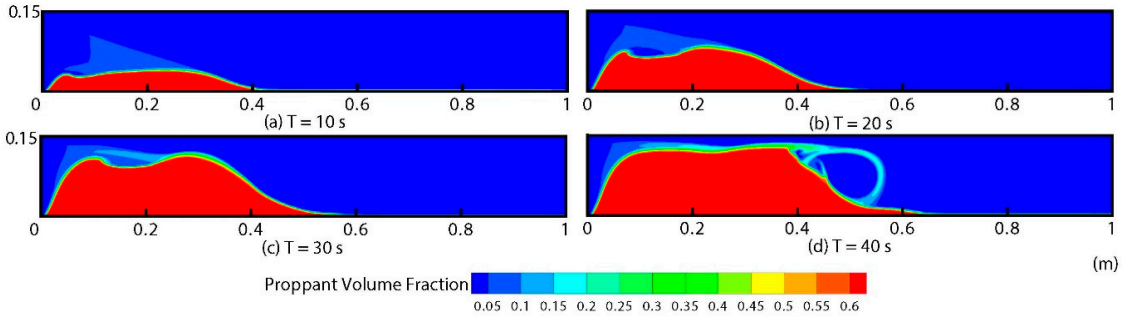


**Figure 2.** The distribution of the proppant in the primary fracture at time (**a**) 10 s, (**b**) 20 s, (**c**) 30 s, and (**d**) 40 s. (Case 3 in Table A1).

In Figure 3a,b, the velocity vector charts of the proppant when the proppant bed height in the primary fracture is about 10% and 75% of the EPH are given (Case 3). The red part of Figure 3 represents the proppant bed. The velocity vector chart of the proppant when the proppant bed moves ahead in primary fracture with the constant bed height is shown in Figure 3c. The proppants settle quickly to the fracture bottom due to the low viscosity of the water initially. As the proppant bed height increases, the following proppants are resisted by the proppant bed and have to move from the upper part of the proppant bed to the depth of the fractures. From the proppant velocity vector chart, it can be found that the proppant bed at the bottom of the fractures does not move. The front part of the bed consists of the following injected proppants, which move forward from the top of the proppant bed surface. Based on the simulation results, the transportation of the proppants in the fractures can be divided into two distinct zones at the steady state: the proppant bed zone and the mixture zone. The mixture zone is the mixture of the proppant and water above the proppant bed.

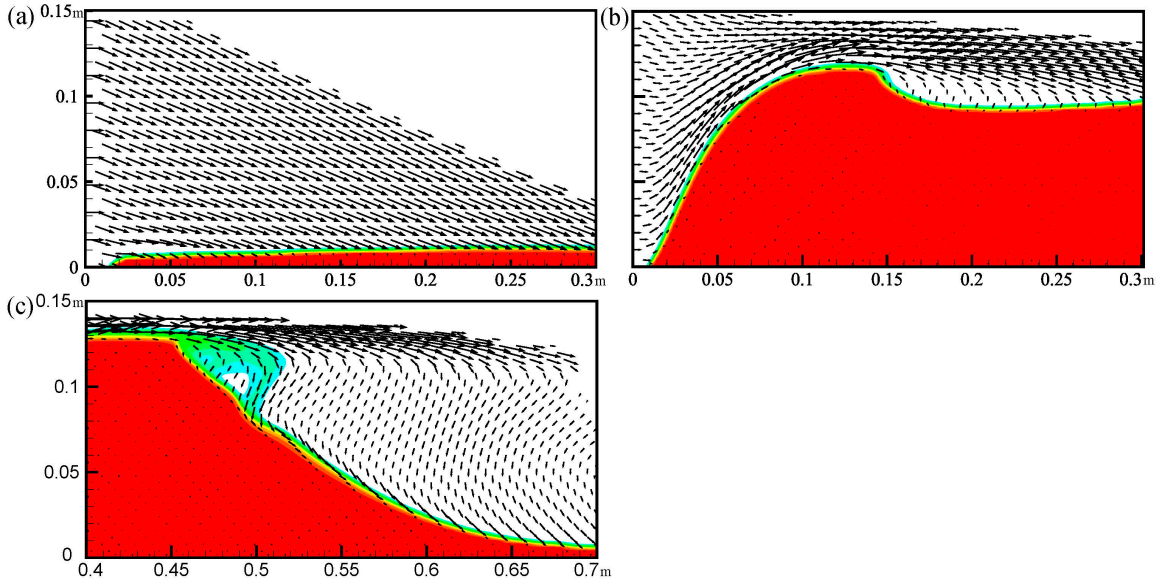


**Figure 3.** The velocity vector charts of the proppant in the primary fracture, (**a**) the proppant bed height is about 0.1 EPH, (**b**) the proppant bed height is about 0.75 EPH, and (**c**) the proppant bed height has reached the EPH. The red part represents the proppant bed. The length and height of the primary fracture is about 1 m and 0.15 m, respectively. The horizontal coordinates indicate the distance from the entrance of the cross fractures. (Case 3 in Table A1). EPH: equilibrium proppant height.

The inlet proppant volume fraction changes from 1% to 11%. Figure 4 shows the change of the relative EPH ($h/H$) with the dimensionless parameters given in Equation (3). The relative EPH increases with the increase of $\alpha_{s0}$ at the value of $\alpha_{s0} < 5\%$ (Figure 4a). When the value of $\alpha_{s0}$ is greater than 5%, the relative EPH becomes stable. Although the relative EPH is constant, the time for the proppant bed height to reach the EPH is shorter due to more proppant injection per unit time. For the field engineering application, a larger proppant inlet volume fraction can be used to achieve a faster stability of EPH. However, a large proppant inlet volume fraction may also lead to the blockage of the fractures.

In the field engineering, the sand ratio ($\varepsilon$) is the ratio of the proppant bulk volume to the water volume. The inlet proppant volume fraction ($\alpha_{s0}$) is the ratio of the proppant volume to the total volume of the proppant and water. The $\alpha_{s0}$ and the $\varepsilon$ values satisfy the relationship $\alpha_{s0} = \xi\varepsilon/(\xi\varepsilon + 1)$, where $\xi$ is the ratio of the bulk density ($\rho_{sb}$) to the real density ($\rho_s$) of the proppant. The sand ratio of the hydraulic fracturing in the field engineering is about 3–8% [21]. Then, the inlet volume fraction of the proppant is about 1–5%. As a result, it can be also concluded that the relative EPH increases with the increase of the sand ratio. According to the simulated results, the most economical sand ratio is about 8%, because the relative EPH becomes stable when the sand ratio is larger than 8%.

The change of the relative EPH with the Reynolds number is shown in Figure 4b. The relative EPH decreases with the increase of the Reynolds number. The Reynolds number characterizes the ratio of the inertia effect to the viscosity effect. A larger Reynolds number causes a higher inertia effect of the proppant and a larger average mixture velocity above the proppant bed. More proppants will be carried far in the fractures. The relative EPH decreases because more proppants on the bed surface move far away in the fractures.

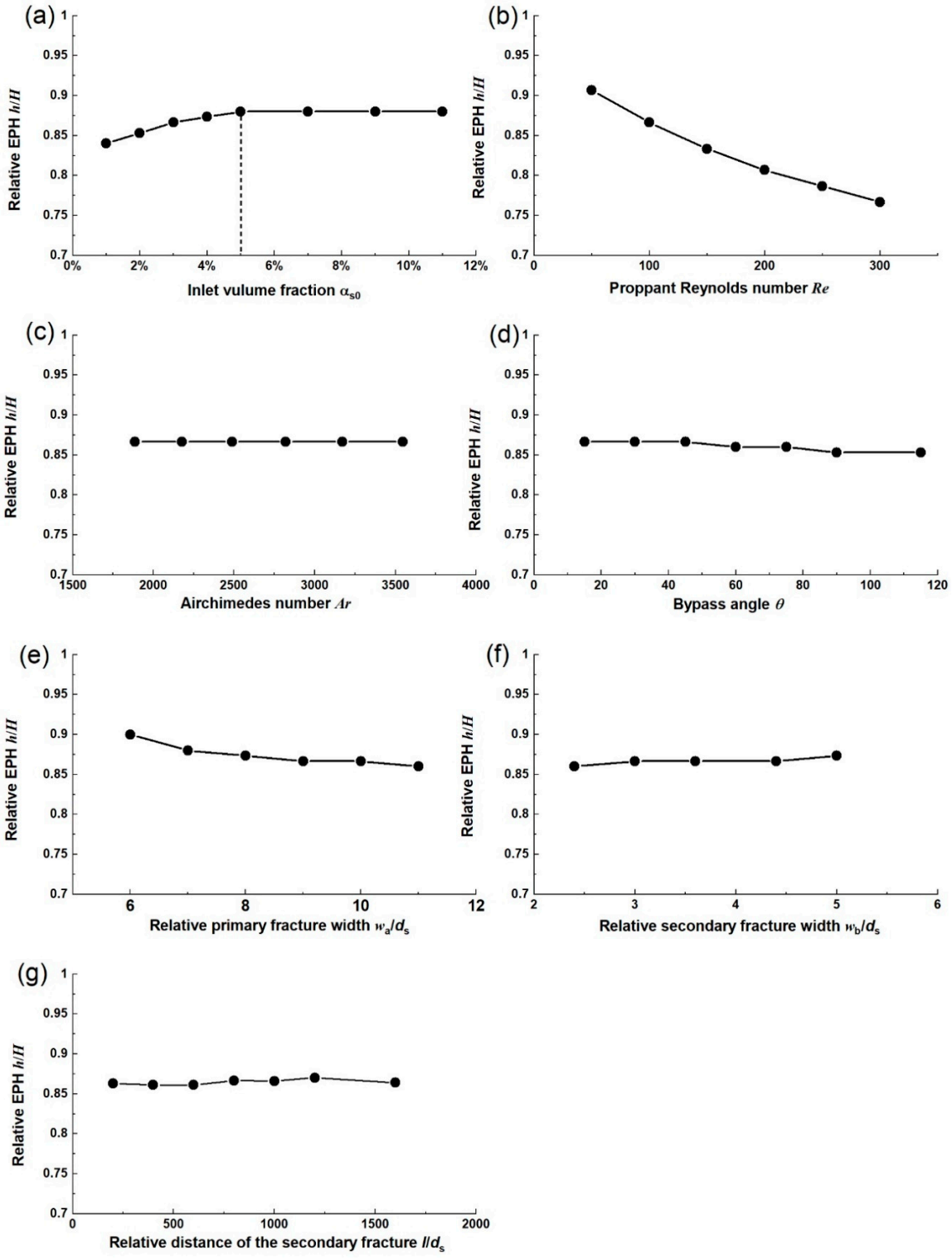


**Figure 4.** The change of the relative EPH with the dimensionless parameters, (**a**) inlet proppant volume fraction, (**b**) proppant Reynolds number, (**c**) Archimedes number, (**d**) angle between primary and secondary fracture (bypass angle), (**e**) relative width of primary fracture, (**f**) relative width of secondary fracture, and (**g**) relative distance of secondary fracture to primary fracture entrance.

Figure 4c,d shows the EPH development with the Archimedes number $Ar$ and the bypass angle $\theta$. The results indicate that the relative EPH changes little with the increase of $Ar$ and $\theta$. The form of the Archimedes number can be written as:

$$Ar = \frac{(\rho_s - \rho_l)\rho_l d_s^3 g}{\mu_l^2} = \frac{\rho_l d_s U_s}{\mu_l} \tag{4}$$

where $U_s = (\rho_s - \rho_l)g d_s^2 / \mu_l$ is related to the settling velocity of a single particle in water [22]. As a result, the Archimedes number can also be called as the proppant settling Reynolds number. It represents the settling effect of the proppant, which mainly affects the sedimentation speed of the proppant in the fractures. The proppants quickly settle to the bottom of the fractures due to the low viscosity of the water after injection (Figure 3a). If the settling effect is enhanced, the time for the proppant bed to reach the EPH will be reduced. Table 2 gives the time for reaching the EPH at different values of the Archimedes number. However, the EPH does not change. The change of the relative EPH with the relative width of the primary and secondary fracture as well as the relative distance of the secondary fracture to the primary fracture entrance are shown in Figure 4e–g. With the increase in the values of $w_a/d_s$, $w_b/d_s$, and $l/d_s$, the relative EPH changes slightly. It can be concluded that the inlet proppant volume fraction and the proppant Reynolds number are the main controlling dimensionless parameters for the relative EPH.

**Table 2.** The time for reaching the EPH at different Archimedes numbers.

| *Ar* | 1888 | 2178 | 2488 | 2820 | 3171 | 3545 |
|---|---|---|---|---|---|---|
| Time/s | 50 | 46 | 43 | 40 | 38 | 36 |

The bypass angle, the relative width of the secondary fracture, and the relative distance of the secondary fracture to the primary fracture entrance are the dimensionless parameters related with the secondary fracture. Comparing Figure 4d–g, it is found that the relative EPH is almost constant with the bypass angle, the relative width of the secondary fracture, and the relative distance of the secondary fracture to the primary fracture entrance. In cross fractures, the secondary fracture has little effect on the proppant transportation in the primary fracture. The reason is that the width of the secondary fracture is always small, and the primary fracture is the main channel for the proppant transportation. That means that previous experiments or numerical simulation results in a single fracture can be extend to the cross fractures.

The proppant Reynolds number, which is also called proppant transport Reynolds number, is divided by the proppant settling Reynolds number:

$$\Pi = \frac{Re}{Ar} = \frac{U_0}{U_s} = \frac{U_0 \mu_l}{d_s^2(\rho_s - \rho_l)g} \tag{5}$$

where $U_0$ is the injection velocity of the mixture. The dimensionless number $\Pi$ is the ratio of the transport effect to the settling effect. Taking the secondary fracture as a single fracture, the average proppant velocity entering the secondary fracture from the primary fracture is set as the transport velocity. Substituting the parameters into Equation (5), the maximum value of $\Pi$ in the secondary fracture is about 0.008 in all the cases, which is much smaller than that in the primary fracture listed in Table A1. This means that the settling effect dominates the movement of proppants in the secondary fracture.

An important issue existing in field engineering is how to transport the proppant from the primary fracture into the subsidiary fracture efficiently. The oil and gas flow through the subsidiary fracture into the primary fracture; then, they are collected in the wellbore. Less proppant transported into the subsidiary fractures will cause the blockage of the seepage flow channel of the oil and gas. It is found that there are two mechanisms for the proppant transporting from the primary fracture into

the secondary fracture [6]. The first one is the gravity effect, and the other one is the water-carrying effect. The gravity is along the vertical direction, and it may not drive the proppant movement to other directions directly. The mechanism of the gravity effect may be that the proppants form a high proppant bed in the primary fracture firstly and then enter the secondary fracture under the gravity effect due to the deposition instability. The water-carrying effect is that the drag force on the proppant forms due to the pressure difference between the fracture entrance and the outlet with water entering the secondary fracture at a certain velocity. Figure 5 gives the formation process of the proppant bed in the secondary fracture (Case 3). When the proppants move to the entrance of the secondary fracture, they directly enter the secondary fracture and slowly build up a proppant bed. Hence, it may be inappropriate to use the gravity effects to explain the proppants entering the secondary fracture, and the fluid-carrying effect may be the main controlling factor.

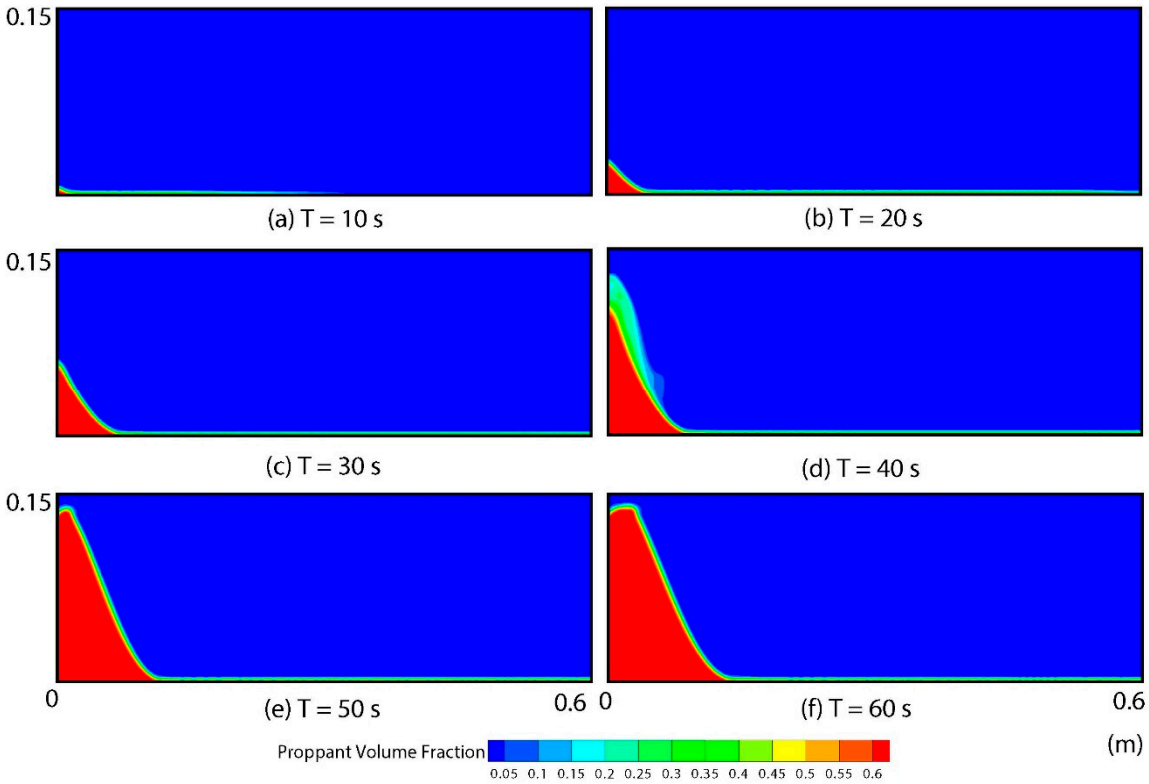


**Figure 5.** The formation process of the proppant bed in the secondary fracture at time (**a**) 10 s, (**b**) 20 s, (**c**) 30 s, (**d**) 40 s, (**e**) 50 s, and (**f**) 60 s. (Case 3 in Table A1).

Figure 6 is a top view of the cross fractures. At the cross section C, the proppants enter from the primary fracture into the secondary fracture. The mass of the proppant in the whole cross fractures and secondary fracture (shaded part in Figure 6) is calculated by the following equation:

$$m_s = \iiint_V \alpha_s \rho_s dV. \tag{6}$$

The RPM can be written as:

$$RPM = \frac{m_{\mathrm{s,sed}}}{m_{\mathrm{s,who}}} = \frac{\iiint_{V_{\mathrm{sed}}} \alpha_s \rho_s dV}{\iiint_{V_{\mathrm{who}}} \alpha_s \rho_s dV} \tag{7}$$

where $m_{\mathrm{s,sed}}$ and $m_{\mathrm{s,who}}$ are the proppants' mass in the secondary and whole cross fractures, respectively. $V_{\mathrm{sed}}$ and $V_{\mathrm{who}}$ are the volume of the secondary fracture and whole cross fractures, respectively.

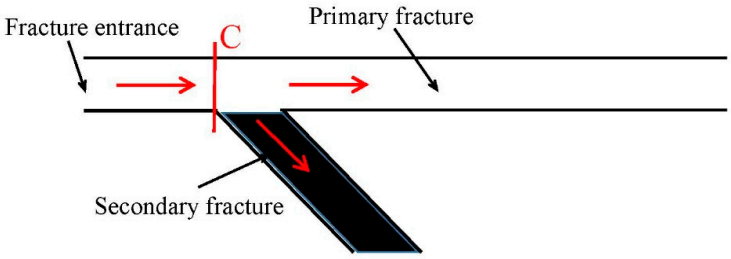


**Figure 6.** A top view of the cross fractures. The shaded part is the secondary fracture.

Figure 7 gives the change of RPM with the dimensionless parameters mentioned in Equation (7). In order to reflect the distribution of the proppants in the primary fracture and the secondary fracture, the RPM is calculated with the same injected mass of the proppant. The RPM curve with the different inlet proppant volume fraction ($\alpha_{s0}$) is shown in Figure 7a. When the inlet volume fraction of the proppant increases, the RPM decreases slightly from 6% to 3%. That means that the increase of the inlet volume fraction does not lead to the increase of the amount of the proppants entering the secondary fracture. More proppants stay in the primary fracture at the large inlet proppant volume fraction. The reason may be that the total resistance of the proppants on the water is larger at the larger inlet proppant volume fraction. The water velocity at the inlet of the secondary fracture is reduced accordingly. As a result, the amount of proppant entering the secondary fracture reduced.

Figure 7b shows the RPM curve with Reynolds number. Similar to the effect of the inlet proppant volume fraction, the RPM decreases from 4.6% to 2.5% with the Reynolds number changing from 50 to 300. The proppants hardly enter the secondary fracture when the Reynolds number is large. The RPM changes little with the Archimedes number and the bypass angle (Figure 7c,d). However, the RPM is greatly influenced by the relative width of the primary and the secondary fracture compared to the $\alpha_{s0}$, $Re$, $Ar$, and $\theta$ (as shown in Figure 7e,f). When $w_a/d_s$ changes from 6 to 11, the RPM decreases from 16% to 3%. This is because when the relative width of the primary fracture is larger, the primary fracture becomes a more favorable channel for the proppant transportation, and more proppants move into the primary fracture, leading to the decrease of the RPM. The RPM increases from 3% to 9% as the value of $w_b/d_s$ changes from 2.4 to 5. When the relative width of the secondary fracture is larger, the possession of the primary fracture is weakened, and more proppants move into the secondary fracture, resulting in the increase of the RPM. If the proppants consist of particles of different diameters, the coarse particles will tend to stay in the primary fracture, and the fine particles are accessible to the secondary fracture. Sahai et al. [6] also found that the proppants in the secondary fractures are thinner than those in the primary fracture by using the proppants with certain particle size grading to investigate the sorting effect of particles at the intersection of the primary and secondary fracture. In conventional hydraulic fracturing, the naturally ceramsite sand proppants with a certain size grading are used. This may be a good way to improve the hydraulic fracturing and increase the oil and gas recovery. The RPM decreases from 6% to 2.3% with the relative distance of the secondary fracture to the primary fracture entrance increasing from 200 to 1400. This is because the transportation time increases for the proppant entering the secondary fracture when the relative distance of the secondary fracture to the primary fracture entrance increases. When injecting the same mass of proppant, the farther the secondary fracture is from the primary fracture, the less proppant will be transported. It can be concluded that the width of the cross fractures has the greatest impact on the amount of proppant entering the secondary fracture.

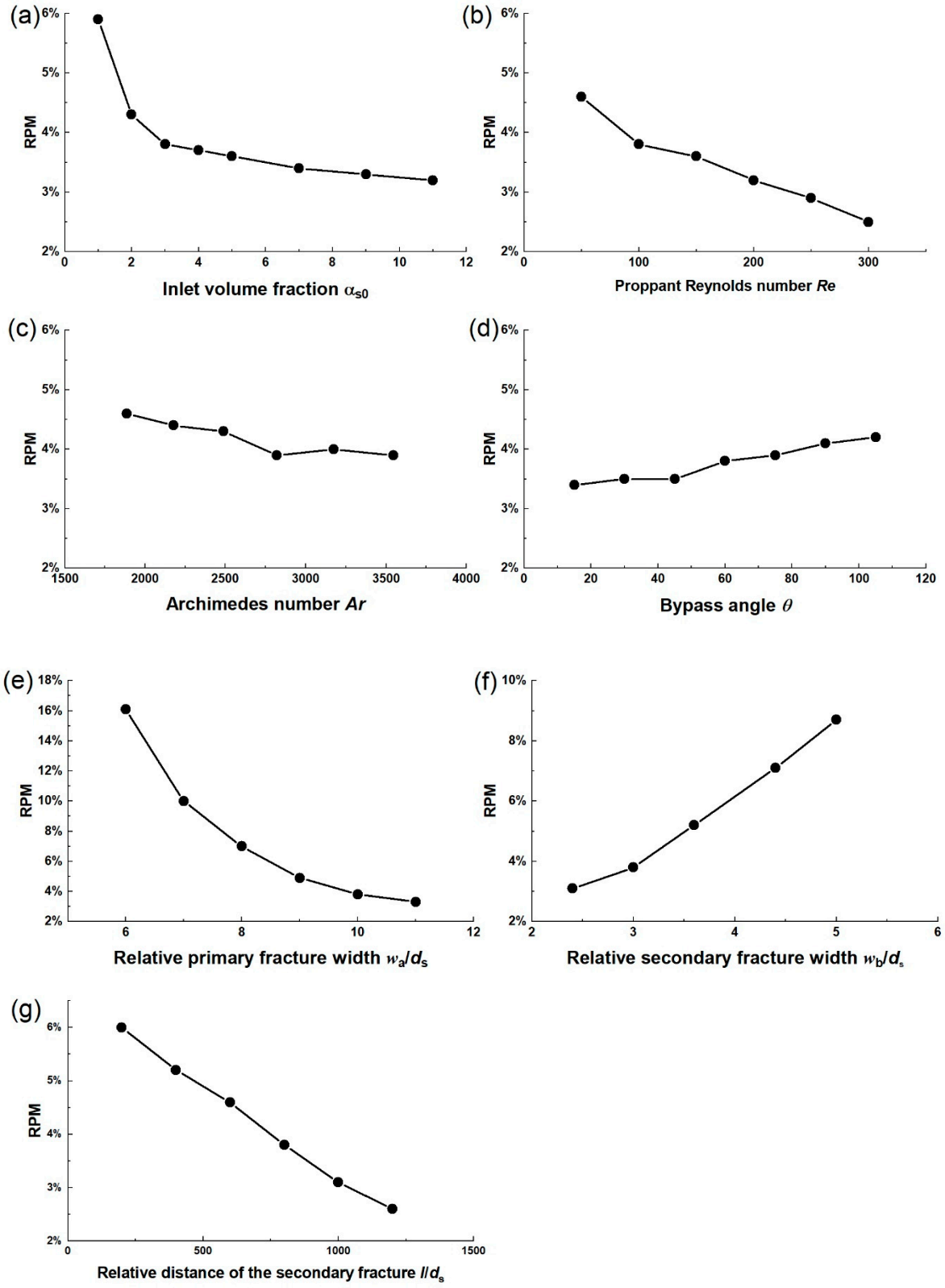


**Figure 7.** The curve of ratio of the proppant mass (RPM) with the dimensionless parameters, (**a**) inlet proppant volume fraction, (**b**) proppant Reynolds number, (**c**) Archimedes number, (**d**) angle between primary and secondary fracture (bypass angle), (**e**) relative width of primary fracture, (**f**) relative width of secondary fracture, and (**g**) relative distance of secondary fracture to primary fracture entrance.

In order to make the numerical simulation results practical for field engineering, more cases are simulated, which are shown in Table A1 (Cases 40–65), and the contour map of RPM relating to the dimensionless parameters is given in Figure 8. Each black dot in Figure 8 represents a case in Table A1, and the coordinates indicate the value of the dimensionless parameters. The percentage of the proppant entering the secondary fracture can be estimated in field engineering based on Figure 8.

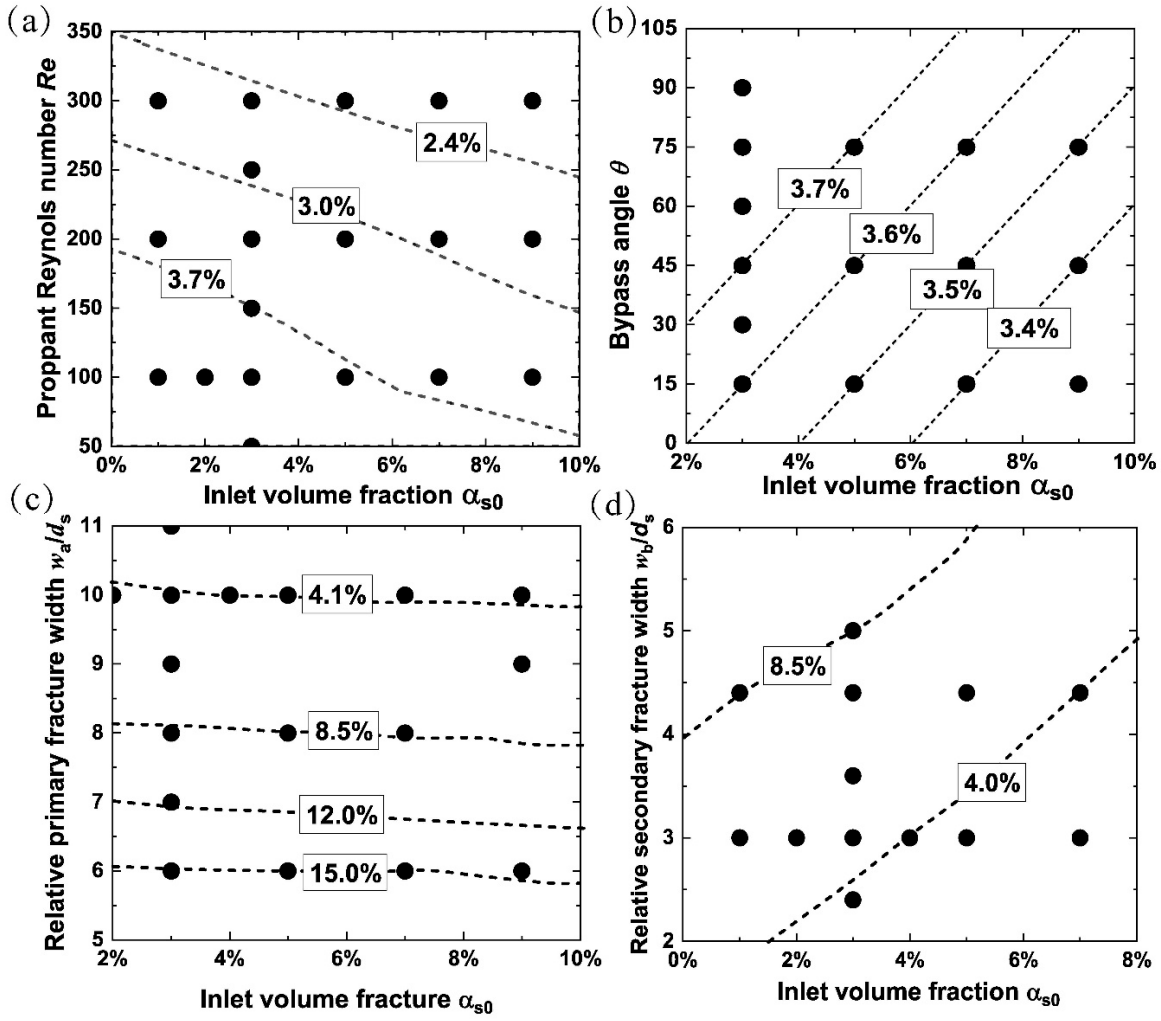


**Figure 8.** The contour map of RPM relating to the dimensionless parameters, (**a**) inlet proppant volume fraction and the proppant Reynolds number, (**b**) inlet proppant volume fraction and the bypass angle, (**c**) inlet proppant volume fraction and the relative width of the primary fracture, (**d**) inlet proppant volume fraction and the relative width of the secondary fracture.

## 4. Conclusions

In this paper, the proppant transportation in the cross fractures is investigated by using the computational fluid dynamics (CFD) method. The Euler–Euler two-phase flow model and the KTFG approach are adopted to describe the flow behaviors. The dimensionless parameters relating to the proppant transportation in the cross fractures, such as the inlet proppant volume fraction, the proppant Reynolds number, the Archimedes number, the bypass angle, the relative width of the primary and secondary fracture, and the relative distance of the secondary fracture to the primary fracture entrance, are derived based on dimensional analysis.

Two dimensionless parameters are proposed to evaluate the distribution of proppants in the cross fractures, i.e., the relative EPH and the RPM. The simulation results show that the main controlling dimensionless parameters for the relative EPH are the inlet proppant volume fraction and proppant Reynolds number. The dominating dimensionless parameters for the RPM are the relative width of the primary and the secondary fracture. The relative EPH decreases with the increase of *Re*, while it increases with the increase of the sand ratio. The admirable sand ratio is about 8% for the field engineering based on the simulation results. When $w_a/d_s$ changes from 6 to 11, the RPM decreases from 16% to 3%. The RPM increases from 3% to 9% when $w_b/d_s$ changes from 2.4 to 5. It is suggested that the proppants with a certain particle size grading may be a good way for improving the hydraulic fracturing and increasing the oil and gas recovery. The settling effect is dominating in the secondary fracture. The proppants enter the secondary fracture mainly under the water-carrying effect. A graph (Figure 8) is given for the engineers to predict the percentage of the proppant entering the secondary fracture.

**Author Contributions:** Conceptualization, Y.Z., X.L. and X.Z.; methodology, Y.Z. P.L. and X.Z.; software, Y.Z. and P.L.; validation, Y.Z. and P.L.; investigation, Y.Z. and X.L.; data curation, Y.Z.; writing—original draft preparation, Y.Z.; writing—review and editing, X.Z. and X.L.; visualization, Y.Z. and P.L.; supervision, X.Z. and X.L.; funding acquisition, X.Z. All authors have read and agreed to the published version of the manuscript.

**Funding:** This research was funded by National Major Oil and Gas Projects of China, grant number 2017X05049003-002 and The APC was funded by National Major Oil and Gas Projects of China.

**Acknowledgments:** This research is supported by the National Major Oil and Gas Projects of China (No.2017X05049003-002). The support is gratefully acknowledged.

**Conflicts of Interest:** The authors declare no conflict of interest.

## Appendix A

**Table A1.** All the cases in the numerical simulation.

| Cases | Proppant | | Water | | Fractures | | | $U_0$/m·s$^{-1}$ | Dimensionless Parameters | | | | | | | |
|---|---|---|---|---|---|---|---|---|---|---|---|---|---|---|---|---|
| | $\rho_s$/kg·m$^{-3}$ | $d_s$/mm | $\rho_l$/kg·m$^{-3}$ | $\mu_l$/Pa·s | $w_b$/mm | $w_a$/mm | $l$/m | | $\alpha_{s0}$/% | $Re$ | $Ar$ | $\theta$/° | $w_a/d_s$ | $w_b/d_s$ | $l/d_s$ | $Re/Ar$ |
| 1 | 3300 | 0.5 | 1000 | $1.0 \times 10^{-3}$ | 1.5 | 5.0 | 0.4 | 0.2 | 1 | 100 | 2820 | 45 | 10 | 3 | 800 | 0.035 |
| 2 | 3300 | 0.5 | 1000 | $1.0 \times 10^{-3}$ | 1.5 | 5.0 | 0.4 | 0.2 | 2 | 100 | 2820 | 45 | 10 | 3 | 800 | 0.035 |
| **3** | **3300** | **0.5** | **1000** | $\mathbf{1.0 \times 10^{-3}}$ | **1.5** | **5.0** | **0.4** | **0.2** | **3** | **100** | **2820** | **45** | **10** | **3** | **800** | **0.035** |
| 4 | 3300 | 0.5 | 1000 | $1.0 \times 10^{-3}$ | 1.5 | 5.0 | 0.4 | 0.2 | 4 | 100 | 2820 | 45 | 10 | 3 | 800 | 0.035 |
| 5 | 3300 | 0.5 | 1000 | $1.0 \times 10^{-3}$ | 1.5 | 5.0 | 0.4 | 0.2 | 5 | 100 | 2820 | 45 | 10 | 3 | 800 | 0.035 |
| 6 | 3300 | 0.5 | 1000 | $1.0 \times 10^{-3}$ | 1.5 | 5.0 | 0.4 | 0.2 | 7 | 100 | 2820 | 45 | 10 | 3 | 800 | 0.035 |
| 7 | 3300 | 0.5 | 1000 | $1.0 \times 10^{-3}$ | 1.5 | 5.0 | 0.4 | 0.2 | 9 | 100 | 2820 | 45 | 10 | 3 | 800 | 0.035 |
| 8 | 3300 | 0.5 | 1000 | $1.0 \times 10^{-3}$ | 1.5 | 5.0 | 0.4 | 0.2 | 11 | 100 | 2820 | 45 | 10 | 3 | 800 | 0.035 |
| 9 | 3300 | 0.5 | 1000 | $1.0 \times 10^{-3}$ | 1.5 | 5.0 | 0.4 | 0.1 | 3 | 50 | 2820 | 45 | 10 | 3 | 800 | 0.018 |
| 10 | 3300 | 0.5 | 1000 | $1.0 \times 10^{-3}$ | 1.5 | 5.0 | 0.4 | 0.3 | 3 | 150 | 2820 | 45 | 10 | 3 | 800 | 0.053 |
| 11 | 3300 | 0.5 | 1000 | $1.0 \times 10^{-3}$ | 1.5 | 5.0 | 0.4 | 0.4 | 3 | 200 | 2820 | 45 | 10 | 3 | 800 | 0.071 |
| 12 | 3300 | 0.5 | 1000 | $1.0 \times 10^{-3}$ | 1.5 | 5.0 | 0.4 | 0.5 | 3 | 250 | 2820 | 45 | 10 | 3 | 800 | 0.088 |
| 13 | 3300 | 0.5 | 1000 | $1.0 \times 10^{-3}$ | 1.5 | 5.0 | 0.4 | 0.6 | 3 | 300 | 2820 | 45 | 10 | 3 | 800 | 0.106 |
| 14 | 2700 | 0.5 | 818 | $1.0 \times 10^{-3}$ | 1.5 | 5.0 | 0.4 | 0.2 | 3 | 100 | 1888 | 45 | 10 | 3 | 800 | 0.053 |
| 15 | 2900 | 0.5 | 879 | $1.0 \times 10^{-3}$ | 1.5 | 5.0 | 0.4 | 0.2 | 3 | 100 | 2178 | 45 | 10 | 3 | 800 | 0.046 |
| 16 | 3100 | 0.5 | 939 | $1.0 \times 10^{-3}$ | 1.5 | 5.0 | 0.4 | 0.2 | 3 | 100 | 2488 | 45 | 10 | 3 | 800 | 0.040 |
| 17 | 3500 | 0.5 | 1060 | $1.0 \times 10^{-3}$ | 1.5 | 5.0 | 0.4 | 0.2 | 3 | 100 | 3171 | 45 | 10 | 3 | 800 | 0.031 |
| 18 | 3700 | 0.5 | 1121 | $1.0 \times 10^{-3}$ | 1.5 | 5.0 | 0.4 | 0.2 | 3 | 100 | 3545 | 45 | 10 | 3 | 800 | 0.028 |
| 19 | 3300 | 0.5 | 1000 | $1.0 \times 10^{-3}$ | 1.5 | 5.0 | 0.4 | 0.2 | 3 | 100 | 2820 | 15 | 10 | 3 | 800 | 0.035 |
| 20 | 3300 | 0.5 | 1000 | $1.0 \times 10^{-3}$ | 1.5 | 5.0 | 0.4 | 0.2 | 3 | 100 | 2820 | 30 | 10 | 3 | 800 | 0.035 |
| 21 | 3300 | 0.5 | 1000 | $1.0 \times 10^{-3}$ | 1.5 | 5.0 | 0.4 | 0.2 | 3 | 100 | 2820 | 60 | 10 | 3 | 800 | 0.035 |
| 22 | 3300 | 0.5 | 1000 | $1.0 \times 10^{-3}$ | 1.5 | 5.0 | 0.4 | 0.2 | 3 | 100 | 2820 | 75 | 10 | 3 | 800 | 0.035 |
| 23 | 3300 | 0.5 | 1000 | $1.0 \times 10^{-3}$ | 1.5 | 5.0 | 0.4 | 0.2 | 3 | 100 | 2820 | 90 | 10 | 3 | 800 | 0.035 |
| 24 | 3300 | 0.5 | 1000 | $1.0 \times 10^{-3}$ | 1.5 | 5.0 | 0.4 | 0.2 | 3 | 100 | 2820 | 105 | 10 | 3 | 800 | 0.035 |
| 25 | 3300 | 0.5 | 1000 | $1.0 \times 10^{-3}$ | 1.5 | 3.0 | 0.4 | 0.2 | 3 | 100 | 2820 | 45 | 6 | 3 | 800 | 0.035 |
| 26 | 3300 | 0.5 | 1000 | $1.0 \times 10^{-3}$ | 1.5 | 3.5 | 0.4 | 0.2 | 3 | 100 | 2820 | 45 | 7 | 3 | 800 | 0.035 |
| 27 | 3300 | 0.5 | 1000 | $1.0 \times 10^{-3}$ | 1.5 | 4.0 | 0.4 | 0.2 | 3 | 100 | 2820 | 45 | 8 | 3 | 800 | 0.035 |
| 28 | 3300 | 0.5 | 1000 | $1.0 \times 10^{-3}$ | 1.5 | 4.5 | 0.4 | 0.2 | 3 | 100 | 2820 | 45 | 9 | 3 | 800 | 0.035 |
| 29 | 3300 | 0.5 | 1000 | $1.0 \times 10^{-3}$ | 1.5 | 5.5 | 0.4 | 0.2 | 3 | 100 | 2820 | 45 | 11 | 3 | 800 | 0.035 |
| 30 | 3300 | 0.5 | 1000 | $1.0 \times 10^{-3}$ | 1.2 | 5.0 | 0.4 | 0.2 | 3 | 100 | 2820 | 45 | 10 | 2.4 | 800 | 0.035 |

**Table A1.** *Cont.*

| Cases | Proppant | | Water | | Fractures | | | $U_0$/m·s$^{-1}$ | Dimensionless Parameters | | | | | | | |
|---|---|---|---|---|---|---|---|---|---|---|---|---|---|---|---|---|
| | $\rho_s$/kg·m$^{-3}$ | $d_s$/mm | $\rho_l$/kg·m$^{-3}$ | $\mu_l$/Pa·s | $w_b$/mm | $w_a$/mm | $l$/m | | $\alpha_{s0}$/% | $Re$ | $Ar$ | $\theta$/° | $w_a/d_s$ | $w_b/d_s$ | $l/d_s$ | $Re/Ar$ |
| 31 | 3300 | 0.5 | 1000 | $1.0 \times 10^{-3}$ | 1.8 | 5.0 | 0.4 | 0.2 | 3 | 100 | 2820 | 45 | 10 | 3.6 | 800 | 0.035 |
| 32 | 3300 | 0.5 | 1000 | $1.0 \times 10^{-3}$ | 2.2 | 5.0 | 0.4 | 0.2 | 3 | 100 | 2820 | 45 | 10 | 4.4 | 800 | 0.035 |
| 33 | 3300 | 0.5 | 1000 | $1.0 \times 10^{-3}$ | 2.5 | 5.0 | 0.4 | 0.2 | 3 | 100 | 2820 | 45 | 10 | 5 | 800 | 0.035 |
| 34 | 3300 | 0.5 | 1000 | $1.0 \times 10^{-3}$ | 1.5 | 5.0 | 0.1 | 0.2 | 3 | 100 | 2820 | 45 | 10 | 3 | 200 | 0.035 |
| 35 | 3300 | 0.5 | 1000 | $1.0 \times 10^{-3}$ | 1.5 | 5.0 | 0.2 | 0.2 | 3 | 100 | 2820 | 45 | 10 | 3 | 400 | 0.035 |
| 36 | 3300 | 0.5 | 1000 | $1.0 \times 10^{-3}$ | 1.5 | 5.0 | 0.3 | 0.2 | 3 | 100 | 2820 | 45 | 10 | 3 | 600 | 0.035 |
| 37 | 3300 | 0.5 | 1000 | $1.0 \times 10^{-3}$ | 1.5 | 5.0 | 0.5 | 0.2 | 3 | 100 | 2820 | 45 | 10 | 3 | 1000 | 0.035 |
| 38 | 3300 | 0.5 | 1000 | $1.0 \times 10^{-3}$ | 1.5 | 5.0 | 0.6 | 0.2 | 3 | 100 | 2820 | 45 | 10 | 3 | 1200 | 0.035 |
| 39 | 3300 | 0.5 | 1000 | $1.0 \times 10^{-3}$ | 1.5 | 5.0 | 0.8 | 0.2 | 3 | 100 | 2820 | 45 | 10 | 3 | 1600 | 0.035 |
| 40 | 3300 | 0.5 | 1000 | $1.0 \times 10^{-3}$ | 1.5 | 5.0 | 0.4 | 0.4 | 1 | 200 | 2820 | 45 | 10 | 3 | 800 | 0.071 |
| 41 | 3300 | 0.5 | 1000 | $1.0 \times 10^{-3}$ | 1.5 | 5.0 | 0.4 | 0.6 | 1 | 300 | 2820 | 45 | 10 | 3 | 800 | 0.106 |
| 42 | 3300 | 0.5 | 1000 | $1.0 \times 10^{-3}$ | 1.5 | 5.0 | 0.4 | 0.4 | 5 | 200 | 2820 | 45 | 10 | 3 | 800 | 0.071 |
| 43 | 3300 | 0.5 | 1000 | $1.0 \times 10^{-3}$ | 1.5 | 5.0 | 0.4 | 0.6 | 5 | 300 | 2820 | 45 | 10 | 3 | 800 | 0.106 |
| 44 | 3300 | 0.5 | 1000 | $1.0 \times 10^{-3}$ | 1.5 | 5.0 | 0.4 | 0.4 | 7 | 200 | 2820 | 45 | 10 | 3 | 800 | 0.071 |
| 45 | 3300 | 0.5 | 1000 | $1.0 \times 10^{-3}$ | 1.5 | 5.0 | 0.4 | 0.6 | 7 | 300 | 2820 | 45 | 10 | 3 | 800 | 0.106 |
| 46 | 3300 | 0.5 | 1000 | $1.0 \times 10^{-3}$ | 1.5 | 5.0 | 0.4 | 0.4 | 9 | 200 | 2820 | 45 | 10 | 3 | 800 | 0.071 |
| 47 | 3300 | 0.5 | 1000 | $1.0 \times 10^{-3}$ | 1.5 | 5.0 | 0.4 | 0.6 | 9 | 300 | 2820 | 45 | 10 | 3 | 800 | 0.106 |
| 48 | 3300 | 0.5 | 1000 | $1.0 \times 10^{-3}$ | 1.5 | 5.0 | 0.4 | 0.2 | 5 | 100 | 2820 | 15 | 10 | 3 | 800 | 0.035 |
| 49 | 3300 | 0.5 | 1000 | $1.0 \times 10^{-3}$ | 1.5 | 5.0 | 0.4 | 0.2 | 5 | 100 | 2820 | 45 | 10 | 3 | 800 | 0.035 |
| 50 | 3300 | 0.5 | 1000 | $1.0 \times 10^{-3}$ | 1.5 | 5.0 | 0.4 | 0.2 | 5 | 100 | 2820 | 75 | 10 | 3 | 800 | 0.035 |
| 51 | 3300 | 0.5 | 1000 | $1.0 \times 10^{-3}$ | 1.5 | 5.0 | 0.4 | 0.2 | 7 | 100 | 2820 | 15 | 10 | 3 | 800 | 0.035 |
| 52 | 3300 | 0.5 | 1000 | $1.0 \times 10^{-3}$ | 1.5 | 5.0 | 0.4 | 0.2 | 7 | 100 | 2820 | 45 | 10 | 3 | 800 | 0.035 |
| 53 | 3300 | 0.5 | 1000 | $1.0 \times 10^{-3}$ | 1.5 | 5.0 | 0.4 | 0.2 | 7 | 100 | 2820 | 75 | 10 | 3 | 800 | 0.035 |
| 54 | 3300 | 0.5 | 1000 | $1.0 \times 10^{-3}$ | 1.5 | 5.0 | 0.4 | 0.2 | 9 | 100 | 2820 | 15 | 10 | 3 | 800 | 0.035 |
| 55 | 3300 | 0.5 | 1000 | $1.0 \times 10^{-3}$ | 1.5 | 5.0 | 0.4 | 0.2 | 9 | 100 | 2820 | 45 | 10 | 3 | 800 | 0.035 |
| 56 | 3300 | 0.5 | 1000 | $1.0 \times 10^{-3}$ | 1.5 | 5.0 | 0.4 | 0.2 | 9 | 100 | 2820 | 75 | 10 | 3 | 800 | 0.035 |
| 57 | 3300 | 0.5 | 1000 | $1.0 \times 10^{-3}$ | 1.5 | 3.0 | 0.4 | 0.2 | 5 | 100 | 2820 | 45 | 6 | 3 | 800 | 0.035 |
| 58 | 3300 | 0.5 | 1000 | $1.0 \times 10^{-3}$ | 1.5 | 4.0 | 0.4 | 0.2 | 5 | 100 | 2820 | 45 | 8 | 3 | 800 | 0.035 |
| 59 | 3300 | 0.5 | 1000 | $1.0 \times 10^{-3}$ | 1.5 | 3.0 | 0.4 | 0.2 | 7 | 100 | 2820 | 45 | 6 | 3 | 800 | 0.035 |
| 60 | 3300 | 0.5 | 1000 | $1.0 \times 10^{-3}$ | 1.5 | 4.0 | 0.4 | 0.2 | 7 | 100 | 2820 | 45 | 8 | 3 | 800 | 0.035 |
| 61 | 3300 | 0.5 | 1000 | $1.0 \times 10^{-3}$ | 1.5 | 3.0 | 0.4 | 0.2 | 9 | 100 | 2820 | 45 | 6 | 3 | 800 | 0.035 |
| 62 | 3300 | 0.5 | 1000 | $1.0 \times 10^{-3}$ | 1.5 | 4.5 | 0.4 | 0.2 | 9 | 100 | 2820 | 45 | 9 | 3 | 800 | 0.035 |
| 63 | 3300 | 0.5 | 1000 | $1.0 \times 10^{-3}$ | 2.2 | 5.0 | 0.4 | 0.2 | 1 | 100 | 2820 | 45 | 10 | 4.4 | 800 | 0.035 |
| 64 | 3300 | 0.5 | 1000 | $1.0 \times 10^{-3}$ | 2.2 | 5.0 | 0.4 | 0.2 | 5 | 100 | 2820 | 45 | 10 | 4.4 | 800 | 0.035 |
| 65 | 3300 | 0.5 | 1000 | $1.0 \times 10^{-3}$ | 2.2 | 5.0 | 0.4 | 0.2 | 7 | 100 | 2820 | 45 | 10 | 4.4 | 800 | 0.035 |

## References


1. Tong, S.; Singh, R.; Mohanty, K.K. A Visualization Study of Proppant Transport in Foam Fracturing Fluids. *J. Nat. Gas Sci. Eng.* **2018**, *52*, 235–247. [CrossRef]
2. Osiptsov, A.A. Fluid Mechanics of Hydraulic Fracturing: A Review. *J. Pet. Sci. Eng.* **2017**, *156*, 513–535. [CrossRef]
3. Barati, R.; Liang, J.T. A Review of Fracturing Fluid Systems Used for Hydraulic Fracturing of Oil and Gas Wells. *J. Appl. Polym. Sci.* **2014**, *131*, 40735. [CrossRef]
4. Wang, J.; Elsworth, D. Role of Proppant Distribution on the Evolution of Hydraulic Fracture Conductivity. *J. Pet. Sci. Eng.* **2018**, *166*, 249–262. [CrossRef]
5. Alotaibi, M.; Miskimins, J. Slickwater Proppant Transport in Complex Fractures: New Experimental Findings & Scalable Correlation. In Proceedings of the SPE Annual Technical Conference and Exhibition, Houston, TX, USA, 28–30 September 2015. [CrossRef]
6. Sahai, R.; Miskimins, J.; Olson, K.E. Laboratory Results of Proppant Transport in Complex Fracture Systems. In Proceedings of the SPE Hydraulic Fracturing Technology Conference, The Woodlands, TX, USA, 4–6 February 2014. [CrossRef]
7. McClure, M. Bed Load Proppant Transport During Slickwater Hydraulic Fracturing: Insights from Comparisons between Published Laboratory Data and Correlations for Sediment and Pipeline Slurry Transport. *J. Pet. Sci. Eng.* **2018**, *161*, 599–610. [CrossRef]
8. Hu, X.D.; Wu, K.; Li, G.S.; Tang, J.Z.; Shen, Z.H. Effect of Proppant Addition Schedule on the Proppant Distribution in a Straight Fracture for Slickwater Treatment. *J. Pet. Sci. Eng.* **2018**, *167*, 110–119. [CrossRef]
9. Roostaei, M.; Nouri, A.; Fattahpour, V.; Chan, D. Coupled Hydraulic Fracture and Proppant Transport Simulation. *Energies* **2020**, *13*, 2822. [CrossRef]
10. Li, P.; Zhang, X.H.; Lu, X.B. Numerical Simulation on Solid-Liquid Two-Phase Flow in Cross Fractures. *Chem. Eng. Sci.* **2018**, *181*, 1–18. [CrossRef]
11. Tong, S.; Mohanty, K.K. Proppant Transport Study in Fractures with Intersections. *Fuel* **2016**, *181*, 463–477. [CrossRef]
12. Zhong, W.Q.; Yu, A.B.; Zhou, G.W.; Xie, J.; Zhang, H. CFD Simulation of Dense Particulate Reaction System: Approaches, Recent Advances and Applications. *Chem. Eng. Sci.* **2016**, *140*, 16–43. [CrossRef]
13. Li, P.; Su, J.Z.; Zhang, Y.; Zhang, X.H.; Lu, X.B. The Two Phase Flow of Proppant-Laden Fluid in a Single Fracture. *Mech. Eng.* **2017**, *39*, 135–144. (In Chinese)
14. Patankar, N.A.; Joseph, D.D.; Wang, J.; Barree, R.D.; Conway, M.; Asadi, M. Power Law Correlations for Sediment Transport in Pressure Driven Channel Flows. *Int. J. Multiph. Flow* **2002**, *28*, 1269–1292. [CrossRef]
15. Dogon, D.; Golombok, M. Self-Regulating Solutions for Proppant Transport. *Chem. Eng. Sci.* **2016**, *148*, 219–228. [CrossRef]
16. Liu, Y.; Sharma, M.M. Effect of Fracture Width and Fluid Rheology on Proppant Settling and Retardation: An Experimental Study. In Proceedings of the SPE Annual Technical Conference and Exhibition, Dallas, TX, USA, 9–12 October 2005. [CrossRef]
17. Tan, Q.M. *Dimensional Analysis: With Case Studies in Mechanics*, 1st ed.; Springer: Berlin Heidelberg, Germany, 2011; pp. 7–16.
18. King, G.E. Thirty Years of Gas Shale Fracturing: What Have We Learned? In Proceedings of the SPE Annual Technical Conference and Exhibition, Society of Petroleum Engineers, Florence, Italy, 19–22 September 2010. [CrossRef]
19. Mack, M.; Sun, J.; Khadilkar, C. Quantifying Proppant Transport in Thin Fluids: Theory and Experiments. In Proceedings of the SPE Hydraulic Fracturing Technology Conference, Society of Petroleum Engineers, The Woodlands, TX, USA, 4–6 February 2014. [CrossRef]
20. Huang, X.; Yuan, P.; Zhang, H.; Han, J.H.; Alberto, M.; Bao, J. Numerical Study of Wall Roughness Effect on Proppant Transport in Complex Fracture Geometry. In Proceedings of the SPE Middle East Oil & Gas Show and Conference, Manama, Kingdom of Bahrain, 6–9 March 2017. [CrossRef]

21. Li, N.; Li, J.; Zhao, L.Q.; Luo, Z.F.; Liu, P.L.; Guo, Y.J. Laboratory Testing on Proppant Transport in Complex-Fracture Systems. *SPE Prod. Oper* **2016**, *32*, 4. [CrossRef]
22. Zhang, H.R.; Liang, H.R.; Yan, X.H.; Wang, B.H.; Wang, N. Simulation on Water and Sand Separation from Crude Oil in Settling Tanks Based on the Particle Model. *J. Pet. Sci. Eng.* **2017**, *156*, 366–372. [CrossRef]